

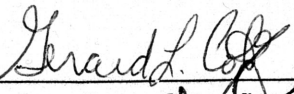
**COMPUTER CLASSIFICATION OF BREAST TUMORS
USING DIGITIZED MAMMOGRAMS**

Kyle M. Allain

University Undergraduate Fellow, 1992-1993
Texas A&M University
Bioengineering Program
Department of Industrial Engineering

APPROVED

Fellows Advisor


Dr. Gerard L. Cote

Honors Director

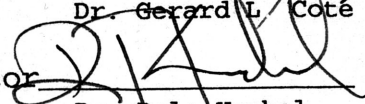

Dr. Dale Knobel

TABLE OF CONTENTS

ABSTRACT	1
I. INTRODUCTION	1
II. FEATURE EXTRACTION	5
A. TUMOR CIRCULARITY	6
B. BOUNDARY ROUGHNESS	7
C. SURFACE ROUGHNESS	8
III. METHODS AND MATERIALS	8
A. MAMMOGRAMS	8
B. IMAGING SYSTEM	9
C. SOFTWARE SELECTION AND DEVELOPMENT	10
D. TUMOR SEGMENTATION	11
E. CIRCULARITY AND SURFACE ROUGHNESS	12
F. BOUNDARY ROUGHNESS	13
IV. RESULTS	16
V. DISCUSSION	18
VI. ACKNOWLEDGEMENTS	21
VII. REFERENCES	22
LIST OF FIGURES AND TABLES	24

ABSTRACT:

A semi-autonomous computer-aided diagnosis system was developed to characterize the distinctions between malignant and benign breast tumors. The scope was limited to two tumor types which are known to have general geometric and histological differences: stellate carcinomas and fibroadenomas. The goal was to construct a user-friendly, modular analysis system capable of using only the information contained in the image to distinguish between the two tumor classes. By analyzing tumor circularity, surface roughness, and boundary roughness, the system was successful in achieving distinct class separation of the sample set of 13 fibroadenomas and 13 stellate carcinomas.

I. INTRODUCTION

Fear of the unknown is one of the more terrifying anxieties that all people must face. In the pathological world, the class of diseases we call 'cancer' induces this fear in its victims. Today, women, as a group, are among those most concerned with cancer because they face a one in nine chance of getting breast cancer in their lifetime [1]. In 1992, an estimated 175,000 women were diagnosed with breast cancer and approximately 44,000 lost their lives to the disease [1]. A proven combatant against this life-threatening disease has been film-screen mammography. When properly performed and the images properly diagnosed, this

imaging procedure has consistently demonstrated its capability for detecting the presence of cancerous tissue at minimally and even pre-invasive stages [2]. Early detection of the cancer is a well-established indicator of the patient's likelihood to survive the invasive disease. Of patients with tumor diameters measuring less than 1.5 centimeters, only 5 to 10% will succumb to the disease within 10 years of the diagnosis [3]. However, for tumors between 2 and 3 centimeters, only 50% of the patients will survive beyond 10 years [3]. Early detection also reduces the need for the emotionally tragic and physically disfiguring mastectomy [4].

Unfortunately, there are many barriers which prevent the benefits of mammography and early detection from being available to all women. Any large-scale screening program is plagued by obstacles in manpower, financing, and technology [5,6,7]. While radiological technicians are licensed to perform the mammogram procedure, the official diagnosis must be done by a doctor who is specially trained in radiology. As this is a costly and subjective limitation on mammography, there has been an initiative in medical research toward developing computer systems which can facilitate interpretation of the film-screens. The ideal system, in absence of a trained radiologist, would locate and classify any tumors that may be present in the mammogram. A computer-based diagnostic tool such as this could operate either autonomously in the ideal case, or,

more practically, under the direction of a radiological technician. Because the computer does not demand an hourly wage, the initial capital investment is diluted as its workload increases. While it would be preferable to have a professional radiologist to view all of the mammograms, the implementation of a large-scale screening program for the entire population will require the use of such technological and cost-saving innovations as the aforementioned computer diagnostic system.

In 1991, the National Cancer Institute assembled to discuss the future of breast imaging [8]. The establishment of a National Digital Mammography Development Group was proposed, whose five primary objectives included the validation and development of neural networks, machine intelligence and novel algorithms to facilitate computer-aided diagnosis of breast tumors [8]. Several research efforts have been conducted in this area both prior to and subsequent to the above proposal. For example, in 1988 Olson and Fam published their work on the detection and analysis of calcifications on film mammograms [9,10]. In 1987, Chan documented the results of his experiments involving the detection of microcalcifications in digital mammography [11]. More recently, there have been publications relating the application of expert systems to the diagnosis of breast tumors. An "Expert Learning System Network for Diagnosis of Breast Calcifications" was described by Patrick in 1991 [12]. Cook and Fox employed an

expert system to integrate user-supplied information such as mammographic observations, patient history, and clinical information [13]. Their rule base was designed to allow people who are not specially trained in radiology or mammography to make a reasonably accurate diagnosis of the tumor type [13]. Kilday submitted a master's thesis to the University of Connecticut in 1991 describing the use of linear discriminant analysis to compile information relating the gross and fine shape descriptors of fibroadenomas, cysts, and cancers [14]. Coté and Fox compared the textures of various tumor surfaces in digitized mammograms by performing the binary joint transform on the intensity patterns of stellate carcinomas, lobule carcinomas, and fibroadenomas [15]. Through the efforts of the researchers mentioned above as well as the significant contributions of others in this challenging field, progress is being made toward the development of an autonomous or at least a semi-autonomous computer system capable of tumor detection and classification. Currently, there exists the need to assimilate the merits of the previous accomplishments in computer-assisted diagnostic mammography into a single system. This study seeks to continue to characterize the differences between malignant and benign tumors based on computerized analysis of the film-screen mammograms. Furthermore, this work introduces the development of a user-friendly, modular software system which will eventually be used as a field diagnostic tool. For the initial

construction of this system, the focus will be on analyzing the geometric and intensity distribution patterns of malignant and benign tumors. Because of its modularity, new levels of complexity can then be added easily later. The releasable product will be a merger between tumor analysis vectors and patient information incorporated into an expert system, providing the user with a high-level diagnostic system.

II. FEATURE EXTRACTION

To facilitate the implementation of the described system, the current task has been limited to the differentiation of two tumors with fairly distinguishable characteristics: stellate carcinomas and fibroadenomas. The stellate mass is most notably characterized by its star-shaped appearance [16]. Its uncircumscribed, spicular border relates the stellate's malignancy as it invades the surrounding breast tissue [16]. The central body of the stellate carcinoma is comprised of fibrous tissue while its activity is in the proliferating cells in the spicules [16]. In contrast to the star-like projections of the stellate carcinoma, the fibroadenoma is usually well circumscribed [16]. Three fibroadenoma images were removed from the study because with the given border detection algorithm they were not circumscribed. The fibroadenoma's border is generally smooth, as it is not malignantly proliferating into the

breast tissue around it. It also has a relatively uniform, low-contrast intensity distribution, which is due to its gross histology [16]. While the characteristics described here are not all-inclusive or exclusively unique, they do provide a general guideline for developing the prototype tumor analysis system.

To properly analyze a breast tumor, it is necessary to obtain a feature vector describing both its boundary and its intensity distribution. The relative roundness of the tumor's boundary is, in this study, represented by tumor circularity. Boundary roughness is measured by the total power contained in the Discrete Fourier Transform of the perimeter. The standard deviation of the pixel values within the tumor was selected to highlight the histological differences in intensity uniformity between the stellates and the fibroadenomas, yielding a measure of surface roughness.

A. Tumor Circularity

Circularity is a standard image processing tool used to represent the roundness of a selected object. Because this study seeks to differentiate the star-like stellate carcinoma border from the relatively round border of the fibroadenoma, circularity should be a useful measure. Supported by its utility in other studies, circularity is defined here as

$$C_i = \frac{P_i^2}{A_i} \quad (1)$$

where P_i is the perimeter and A_i is the area of i^{th} tumor [14].

B. Boundary Roughness

While the circularity feature is valuable as a general geometric descriptor, it is necessary also to have a measure of the relative 'roughness' of a tumor's boundary. A radial representation of the boundary was obtained and mapped into a one-dimensional vector. The measure of 'roughness' is generated by performing the one-dimensional Discrete Fourier Transform (DFT) of these values. By summing the squares of the magnitudes of the DFT, a total power was calculated for the boundary of the i^{th} tumor as [17]:

$$P_{\text{Tot}_i} = \sum_{u=0}^M |D(u)|^2 \quad (2)$$

$$D(u) = \frac{1}{M} \sum_{i=0}^{M-1} d_i \exp(-j2\pi ui/M) \quad (3)$$

where d_i is the deviation of the i^{th} boundary coordinate from the average radius of the tumor, M is the total number of points used to represent the tumor boundary, $D(u)$ is the Discrete Fourier Transform of the radial deviation vector,

and P_{Tot_i} is the total spectral power of the i^{th} tumor boundary.

C. Surface Roughness

Because the fibroadenoma differs from the stellate carcinoma in that it is histologically noted for its smooth, uniform surface, the standard deviation of the pixel intensity values within the tumor boundaries is used to reflect the degree of surface roughness:

$$\sigma_i = \sqrt{\frac{1}{N} \sum_{x \in T} \sum_{y \in T} (f(x,y) - \bar{f}(x,y))^2} \quad (4)$$

where σ_i is the standard deviation of the intensity values of the N pixels enclosed by the boundary of the i^{th} tumor, $f(x,y)$ is the intensity value of a point that is considered to be part of the tumor (T), and $\bar{f}(x,y)$ is the average intensity value within the tumor.

III. METHODS AND MATERIALS

A. Mammograms

The film-screen mammograms¹ from a single patient constitute a set of films. Each set generally contained four films, representing both the right and left mediolateral and craniocaudal views. Twenty-one mammography

sets contained tumors which were previously diagnosed as stellate carcinomas. A total of 20 sets contained images of clinically diagnosed fibroadenomas. Among the entire library of film-screens, 12 carcinoma sets and 5 fibroadenoma sets were rejected because the tumor was either not discernible or was not completely contained within the film-screen. All of the images in this experiment were the original film-screens.

B. Imaging System

A standard white-light transilluminator with a light-diffusing surface illuminated the X-rays. In order to minimize the amount of stray light entering the optical system, an opaque shroud with a small rectangle excised was placed over the viewing box. Also, the lights in the digitizing room were turned off during the capturing procedure. These practices, combined with the diffusing screen on the transilluminator, yielded an extremely uniform backfield illumination for which no background subtraction was required. The film-screens were translated to a digital picture of 256 grey levels by using a 50mm lens to focus the radiated light pattern onto the photoreceptor field of a model JE2062IR Javelin MOS Solid State Video Camera. To achieve maximum magnification, the lens was focused at its minimum focal depth of approximately 1.5 feet. The lens yielded an approximate 3.5 to 1 magnification ratio, which was mapped into the 640 by 480 pixel matrix of the frame-

grabbing board. These parameters combine to produce a resolution of 10 pixels/mm. In order to reduce the noise introduced by the scanning nature of the camera, 50 frames were averaged for each archived image. Because of the great variability in the contrast levels and maximum intensities of the different film-screens, it was not desirable to keep the lens aperture fixed. Instead, the aperture was adjusted for each image such that the resulting image was not saturated and the dynamic range was maximized. An illustration of the imaging system appears in Figure 1. In a finalized analysis system, it would be possible to bypass the film digitization procedures by directly importing the digital information from the X-ray mammography unit.

C. Software Selection and Development

As one of the primary goals of this project is to construct the foundation of a user-friendly, modular, inexpensive computer diagnostic tool, the selection of the imaging software was a critical decision. It was most desirable to choose a software package which provided a strong image display and manipulation environment while also allowing the complete integration of user-defined functions. Furthermore, if the costs of a final system are to be minimized, then the computer itself must also be affordable. For this reason, the experiments were performed on a Macintosh IIX computer. The imaging software shell selected was *Image 1.44*, developed as a share-ware research tool by

Wayne Rasband at the National Institute of Health. *Image's* principle advantage is that its Pascal source code is freely circulated by its developer. Using Symantec Corporation's *Think Pascal 4.0* for the Macintosh, it was possible to incorporate the image processing techniques outlined in this experiment into customized pull-down menus. Special analysis algorithms were designed to implement the circularity and boundary roughness calculations. These functions were developed as separate Pascal units and were fully integrated into the *Image* shell. Another advantage of using *Image* is that the parameters of the processing algorithms can be easily altered through the use of 'pop-up' boxes, allowing for analysis over a wide range of variability. Also, the results can be presented immediately after each processing function, and in any form the programmer desires.

D. Tumor Segmentation

The first phase in the analysis of any tumor is segmentation. Because the tumors are generally denser than the surrounding breast tissue, they are represented in the digitized film-screens by higher intensity pixel values. Fairly successful segmentation was obtained by using *Image's* built-in density slicing function. Density slicing is a technique in which a specified intensity range of a grey-scale image is highlighted in a non-grey color such as red. For tumor segmentation, the upper end of the density slice

was fixed at 255 while the lower end was manually adjusted such that a reasonable representation of the tumor was highlighted. The boundary around the tumor was easily obtained by using the Macintosh mouse and *Image's* 'wand' selection tool to select the appropriate density-sliced region as the 'region of interest'. While this method of segmentation proved to be adequate for the majority of the tumors, it was not able to segment all of them. Due to the limitations of this tumor isolation technique, one of the carcinoma views and 10 of the fibroadenoma views were removed from the study due to poor segmentation. However, satisfactory segmentation was achieved on a total of 13 carcinoma views and 13 fibroadenoma views, which comprise the data set of this study. The tumor outlines resulting from segmentation are shown in Figure 2 (stellate carcinomas) and Figure 3 (fibroadenomas).

E. Circularity and Surface Roughness

Once the tumor has been segmented and selected as the 'region of interest', *Image's* built in 'Measure' command can be invoked to calculate the perimeter length and area of the tumor. The units for both measurements are whole pixels. The circularity feature is then calculated with the aid of a Pascal unit created by the investigator which accesses *Image's* internal parameters for perimeter length and area. The perimeter is squared and divided by the area, and the result is immediately relayed to the user through a pop-up

message box. It is important to make the distinction that the Pascal unit which allows access to, processing of, and display of the desired information on tumor features is a completely separate sub-program which has been created by the investigator and compiled into the source code of the *Image* application. *Image*'s 'Measure' command will also calculate the standard deviation of the pixel intensity values enclosed within the tumor boundary. Through the investigator-defined Pascal unit interface, this standard deviation parameter is accessed and displayed to the user as an indicator of surface roughness.

F. Boundary Roughness

While the circularity and surface roughness features are fairly direct calculations, the boundary roughness measure is more complex. The first obstacle to obtaining this information is to acquire an accurate coordinate mapping of the tumor boundary. Unfortunately, *Image* does not record its boundary information as a list of neighboring pixels. *Image*'s border data is stored instead as an x,y paired array of points connected by lines. For example, if the boundary encloses a 10 pixel by 10 pixel square, *Image*'s internal representation would not necessarily be 40 pixels but could be as few as four, which are known to be linked by straight lines. To overcome the limitations of this internal data structure, a separate procedure was created to interpolate between each pair of points that are not 8-

neighbors. In order to keep the spacing of the new boundary coordinates uniform, the interpolation is performed such that the distance between two successive coordinate pairs is approximately one pixel. The coordinates of this interpolated boundary representation are generated by an investigator-created Pascal procedure and stored as an array of records containing the x and y locations of the points comprising the boundary. Information on the centroid of the area enclosed by the tumor boundary is acquired by executing Image's 'XY center' option under the 'Measure' menu. This data is combined with the boundary coordinates to calculate the tumor's average radius:

$$R_i = \frac{1}{M} \sum_{j=0}^{M-1} \sqrt{[(b_{j_x} - x_o)^2 + (b_{j_y} - y_o)^2]} \quad (5)$$

where R_i is the average radius of the i^{th} tumor, M is the total number of boundary coordinates, x_o and y_o are the x,y center of the tumor, and b_{j_x} and b_{j_y} represent the x,y location of the j^{th} element of the boundary coordinate list.

Because of the great variability in tumor sizes, the calculated average radius is used as a means of normalization. Each tumor is linearly scaled by a scaling factor, s_{f_i} , such that it will have a new average radius of 80 pixels:

$$S_{f_i} = \frac{80}{R_i} \quad (6)$$

If a tumor has a scaling factor greater than one, then it is smoothed by a 3x3 lowpass averaging filter prior to further processing. The boundary of the normalized tumor is computed using the same density slicing and interpolation techniques described above.

In order to perform the Fourier analysis of the tumor boundary, it is necessary to convert the two-dimensional visual representation to a one-dimensional vector containing the Euclidean distance between each boundary coordinate and the tumor's centroid. For comparative purposes, it is desirable to have all of the sequences be of the same length. To achieve these specifications, the array of interpolated boundary coordinate radial lengths for each tumor is sampled to yield a similar array of 1024 samples. Prior to the Fourier analysis of this mapping, the average radius of the scaled tumor (~80 pixels) is subtracted such that the mean value of the input signal is zero. Because the size of the sample set is a power of 2, the spectral analysis is rapidly performed by using the Fast Fourier Transform algorithm [17]. The total power of the resulting Fourier spectrum for each tumor boundary is calculated and used as a measure of boundary roughness. Figure 4 illustrates the procedures involved in obtaining the total spectral power of a tumor border. Like the previous feature

descriptors, the procedures involved in its calculation and representation have been developed as independent Pascal sub-programs and integrated into the *Image* shell as investigator-created menu options.

IV. RESULTS

The results generated by the computer diagnostic tool developed for this study are tabulated in Table 1 (stellate carcinomas) and Table 2 (fibroadenomas). The average circularity of the 13 stellate tumors in this study was 77.60 with a standard deviation of 22.98. The 13 fibroadenoma tumors had an average circularity of 52.07 and a standard deviation of 11.35. Recalling that circularity is a measure of the perimeter squared divided by the area of the tumor, the data indicates that, as expected, the fibroadenomas are closer than the carcinomas to the perfect circularity value of 4π .

The surface roughness feature, which is measured by the standard deviation of the pixel intensity values enclosed within the tumor boundaries, revealed that the fibroadenomas, as anticipated, had considerably smoother surfaces than the stellate carcinomas. The fibroadenomas had an average surface roughness value of 10.02 ($\sigma=5.34$), compared to a much higher average value of 20.61 ($\sigma=8.19$) for the carcinomas.

The final parameter employed to differentiate the tumors is the spectral analysis of the deviation of the points on the tumor boundary from the tumor's calculated average radius. By summing the resulting power spectrum of each tumor, a measure of boundary roughness is obtained. With an average boundary roughness value of 315.86 ($\sigma=135.65$), the stellate carcinomas had a rougher, more variant border than the fibroadenomas. The relative smoothness of the fibroadenoma borders was reflected by their mean roughness value of only 129.54 ($\sigma=96.78$).

The relationships between these three tumor features are illustrated in Figures 5,6,7, and 8. Figure 5 plots surface roughness against circularity. With only mild intermixing, the fibroadenomas and stellate carcinomas lie in separate, distinct clusters. Figure 6 illustrates the relationship between the boundary roughness and circularity of the two tumor types. As in Figure 5, the carcinomas and fibroadenomas precipitate into two different clusters. Figure 7 reveals that comparing surface roughness to boundary roughness does not contain as much class distinction as the other relationships. Finally, Figure 8 coalesces all of the elements of the feature vector into a three-dimensional representation. Through the aid of this visualization, it becomes apparent that the features calculated by this study clearly separate the fibroadenomas and stellate carcinomas into two distinct classes.

V. DISCUSSION

The compiled data of this study supports the known histological and geometric differences between stellate carcinomas and fibroadenomas. The greater mean circularity value for the carcinomas coincides with their star-shaped appearance, which gives the tumor a much larger perimeter to area ratio than the rounder fibroadenoma. The fibroadenoma tumors are generally composed of tissue which is of uniform density, giving them a smooth surface texture [16]. However, no such surface uniformity distinction is given for the stellate carcinomas, which implies that their surface textures are greatly varied. These statements are supported by the data, which indicates the fibroadenomas have a surface which is only one-half the roughness of the stellate carcinomas. Because the stellate tumors are malignant, it is expected that their borders would be much rougher and more jagged than those of the non-invasive, benign fibroadenomas. This pathologic characteristic is reflected in the data, which indicates that the mean boundary roughness of the carcinomas is more than twice that of the fibroadenomas.

The success of this study lies not only in its positive results, but also in the design of the system from which they were obtained. The entire analysis procedure was performed without exiting the *Image* software shell. Furthermore, the end user is isolated from the intricacies

of the processing algorithms because the functions are executed by selecting investigator-created menu choices. The user is required only to digitize the film-screen, select the most appropriate density slice, 'click' on the tumor with *Image's* 'wand' tool, and execute the processing functions which have been incorporated into a menu. The values calculated for each feature are then immediately presented to the user in a message box. This user-friendly, integrated design is a great advantage over other systems which require the use of several different software packages and/or hardware units. Furthermore, the modularity with which this system was designed allows higher levels of diagnostic complexity to be added easily without increasing the burden on the user.

Perhaps the most limiting factor on this study of stellate carcinomas and fibroadenomas was the tumor segmentation procedure. While the density slicing technique was adequate for most of the tumors, there is a clear need for the development of a segmentation algorithm which would provide accurate segmentation for all tumors. Once such a procedure is developed, it can be inserted into this system and used in conjunction with the feature analysis functions.

The next phase of this on-going project involves several parallel research pursuits. One of the more important tasks is, as mentioned previously, to design a more accurate and objective tumor segmentation algorithm. It is also necessary to continue the testing of the current

system by expanding the data set beyond the 26 views which were analyzed in this study. New relationships between the stellate carcinomas and fibroadenomas should be explored and implemented so that the classes can be distinguished with a greater confidence level. The output parameters of this system should be linked to an expert system which can be trained to assimilate the data, include patient history information, and make a high-level classification decision by weighting the various inputs. Also, more tumor types should be introduced into future studies to expand the system's diagnostic utility.

As new ideas and innovations continue to develop in this field of computer-aided diagnosis of breast images, the creation of an inexpensive, reliable, automated tumor analysis system will indeed become a reality. With the development and production of such a system, mammographic screening can be extended to many more women and ultimately save many more lives.

VI. ACKNOWLEDGEMENTS

I would like to thank all those who gave generously of their time and resources to make this project a success: Dr. Gerard Coté as my mentor and advisor, Dr. Joe Pruneda for supplying the mammograms, Dr. Nasser Khetarnavaz for his technical assistance on Fourier spectral analysis, and Dr. Joe Foster for supplying the digitizing and processing equipment.

VII. REFERENCES

- [1] American Cancer Society, *Cancer Facts and Figures-1992*, 1992.
- [2] Lester, R.G., M.D. "The Contributions of Radiology to the Diagnosis, Management, and Cure of Breast Cancer.", *Radiology*, 151:1-7, 1984.
- [3] Bjurstam, N., "The Value of Mammography in Estimating the Prognosis for Patients with Breast Cancer.", *Recent Results Cancer Res.*, 90:173, 1984.
- [4] Zhou, X.H., Gordon, R., "Detection of Early Breast Cancer: An Overview and Future Prospects.", *Critical Review in Biomedical Engineering*, 17(3):203-255, 1989.
- [5] Hall, F.M., "Screening Mammography.", *American Journal of Roentgenology*, 147:195, 1986.
- [6] Hall, F.M., "Screening Mammography - Potential Problems on the Horizon.", *New England Journal of Medicine*, 314:53, 1986.
- [7] McLelland, R. "Mammography 1984: Challenge to Radiology", *American Journal of Roentgenology*, 142:1, 1984.
- [8] Shtern, F., M.D., "Digital Mammography and Related Technologies: A Perspective from the National Cancer Institute.", *Radiology*, 183:629-630, 1992.
- [9] Bahaa, W.F., Olson, S.L., Winter, P.F., Scholz, F.J., "Algorithm for the Detection of Fine Clustered Calcifications on Film Mammograms.", *Radiology*, 169:333-7, 1988.
- [10] Olson, S.L., Bahaa, W.F., Winter, P.F., Scholz, F.J., Lee, A.K., Gordon, S.E., "Breast Calcifications: Analysis of Imaging Properties.", *Radiology*, 169:329-32, 1988.

- [11] Chan H., Vyborny, C.J., MacMahon, H., Metz, C.E., Doi, K., Sickles, E.A., "Digital Mammography ROC Studies of the Effects of Pixel Size and Unsharp-Mask Filtering on the Detection of Subtle Microcalcifications.", *Investigative Radiology*, 22:581-589, 1987.

- [12] Partick, E.A., Ph.D., M.D., FACEP, Moskowitz, M., M.D., FACR, Mansukhani, V.T., M.S., Gruenstein, E.I., Ph.D., "Expert Learning System Network for Diagnosis of Breast Calcifications.", *Investigative Radiology*, 26:534-9, 1991.

- [13] Cook, H., Fox, M.D., Ph.D., "Application of Expert Systems to Mammographic Image Analysis.", *American Journal of Physiologic Imaging*, 4:16-22, 1989.

- [14] Kilday, J., *Classifying Mammographic Lesions Using Computerized Image Analysis of Tumor Shape*, M.S. Thesis, University of Connecticut, Storrs, CT., 1991.

- [15] Coté, G.L., Fox, M., M.D., "Differentiation of Mammographic Tumor Types Using the Binary Joint Transform Correlator.", Presented, IEEE EMBS 11th Annual Conference, Seattle, Wa., 1989.

- [16] Martin, J.E. M.D., FACR, *Atlas of Mammography Histologic and Mammographic Correlations - Second Edition*, Williams & Wilkins, 1988.

- [17] Gonzalez, R.C., Woods, R.E., *Digital Image Processing*, Addison-Wesley, 1992.

LIST OF FIGURES AND TABLES

Figure 1: Diagram of imaging system.

Figure 2: Stellate carcinoma segmentation result.

Figure 3: Fibroadenoma segmentation result.

Figure 4: Illustration of procedure used to calculate boundary roughness.

- (a) Segmented tumor.
- (b) Circle of computed average radius superimposed on (a).
- (c) Tumor scaled to an average radius of 80 pixels.
- (d) Plot of Euclidean distance from each boundary coordinate to tumor centroid.
- (e) Plot (d) sampled to 1024 samples.
- (f) Discrete Fourier Transform of (e).

Figure 5: XY scatter plot of surface roughness and circularity.

Figure 6: XY scatter plot of boundary roughness and circularity.

Figure 7: XY scatter plot of surface roughness and boundary roughness.

Figure 8: 3D point plot of circularity, surface roughness, and boundary roughness.

Table 1: Results data for stellate carcinomas.

Table 2: Results data for fibroadenomas.

Hardware Configuration

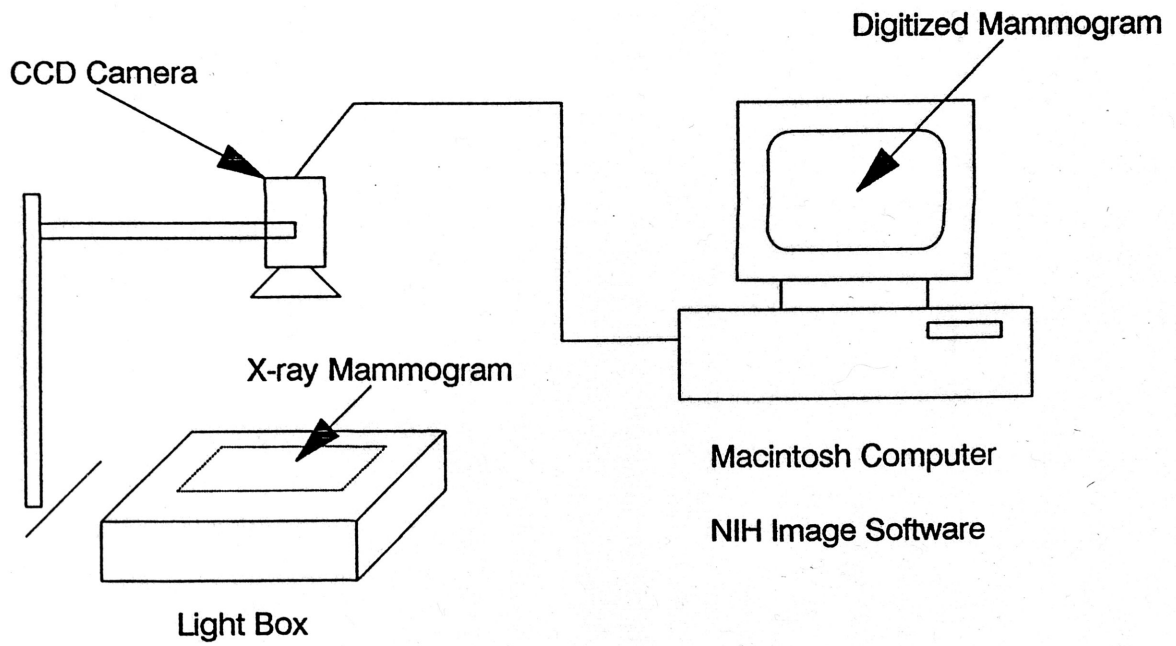


Figure 1. Imaging System

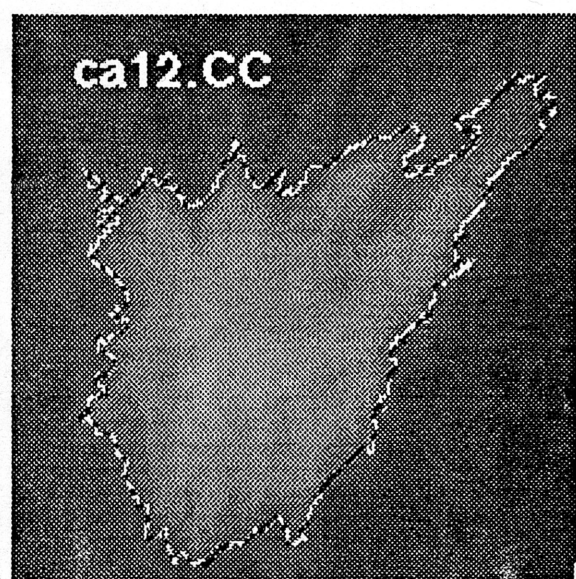
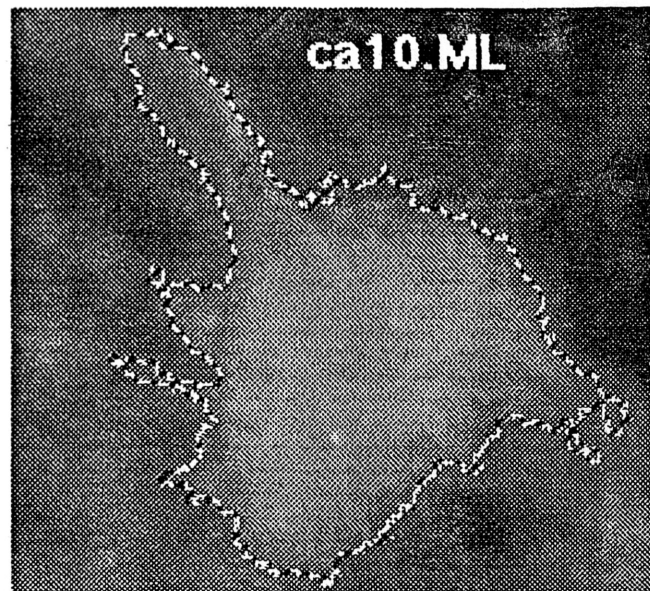
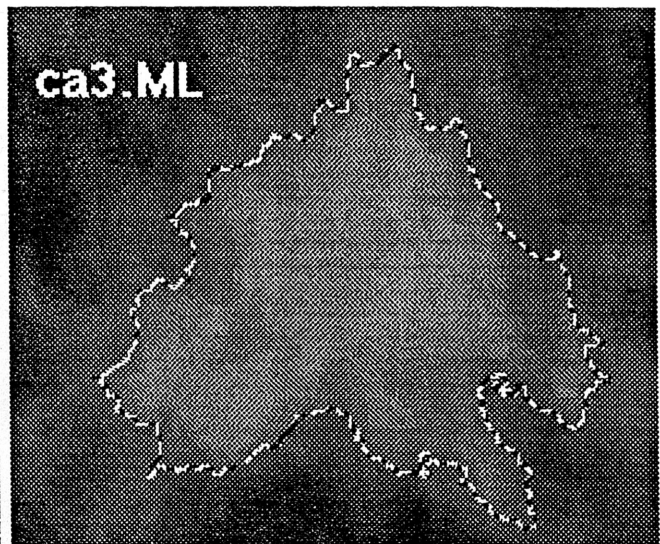
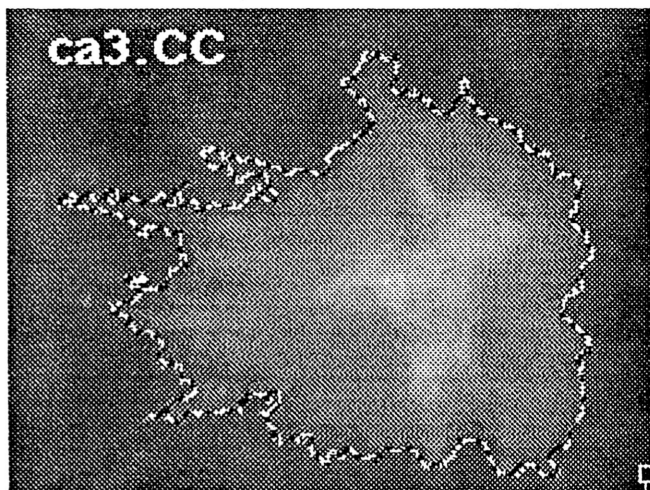
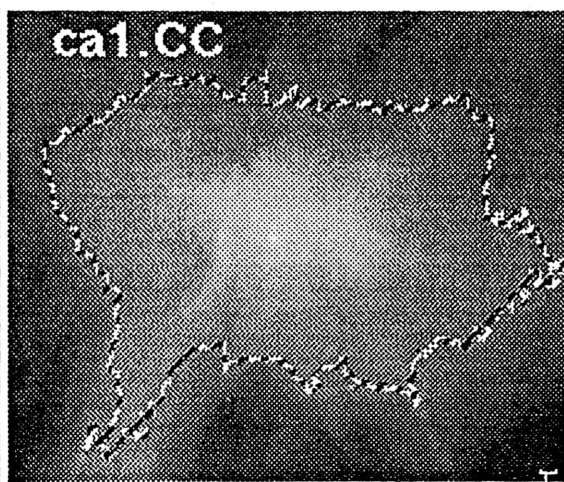
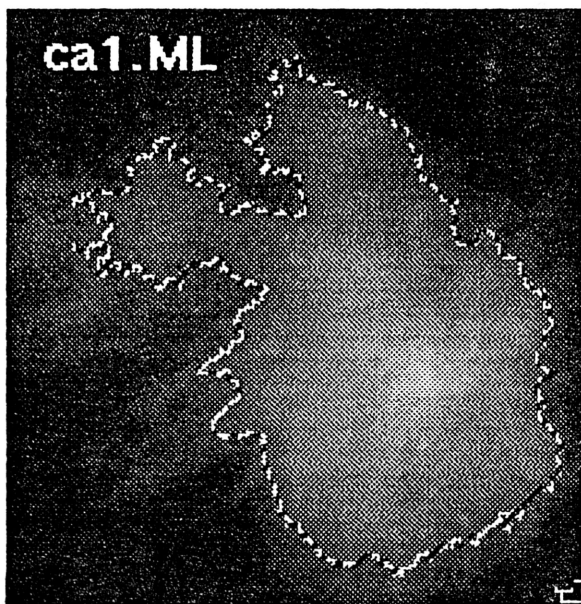
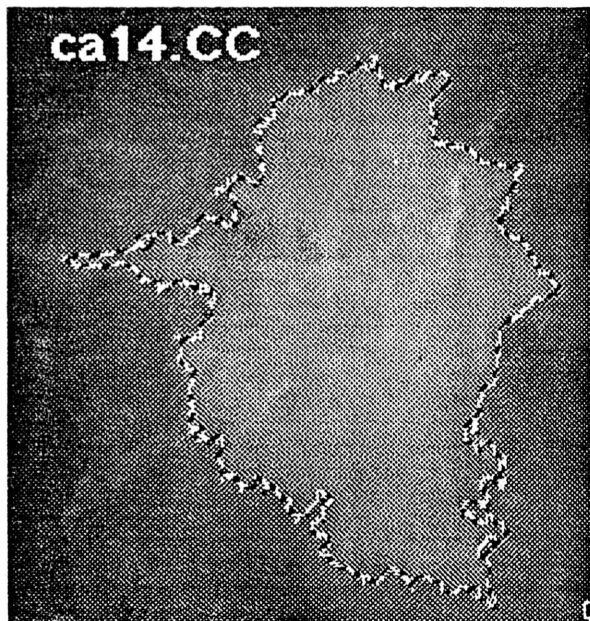
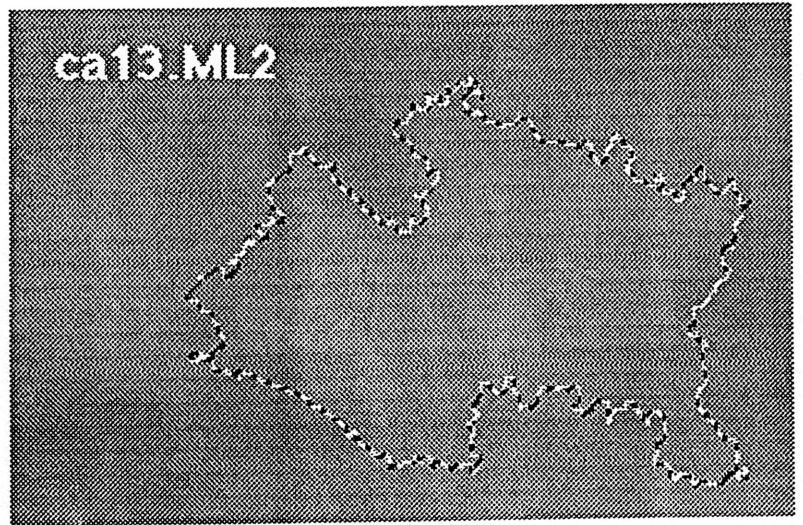
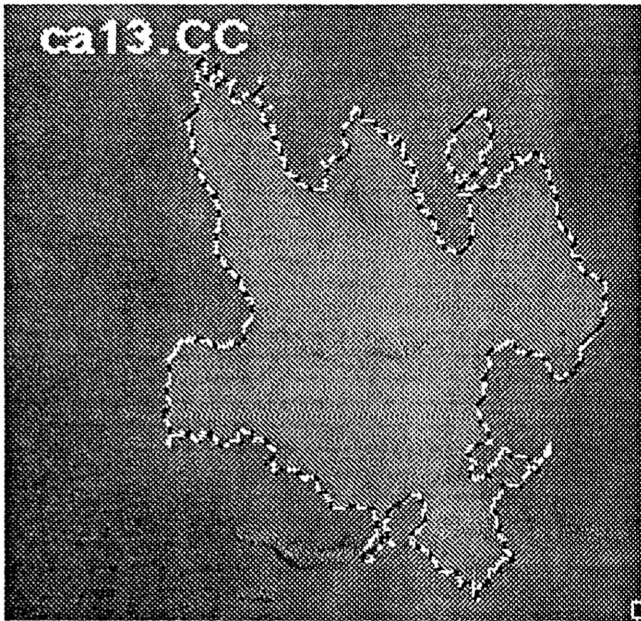
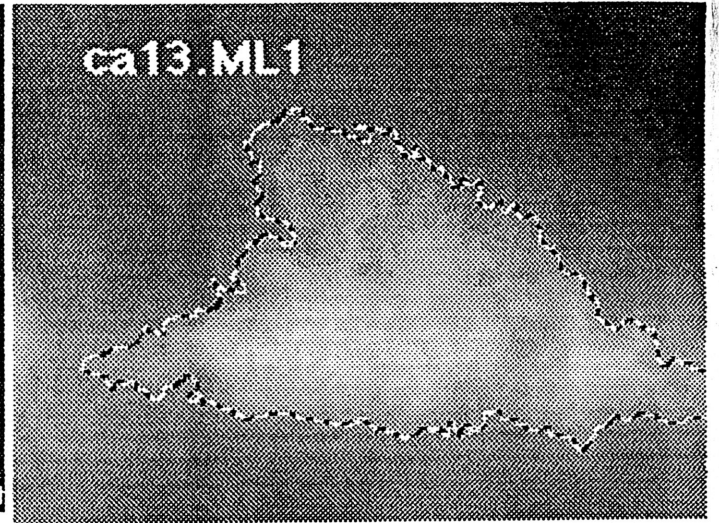
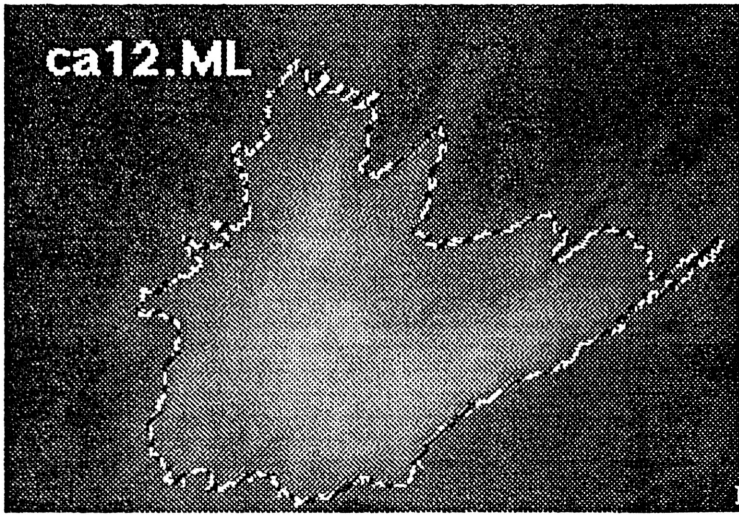
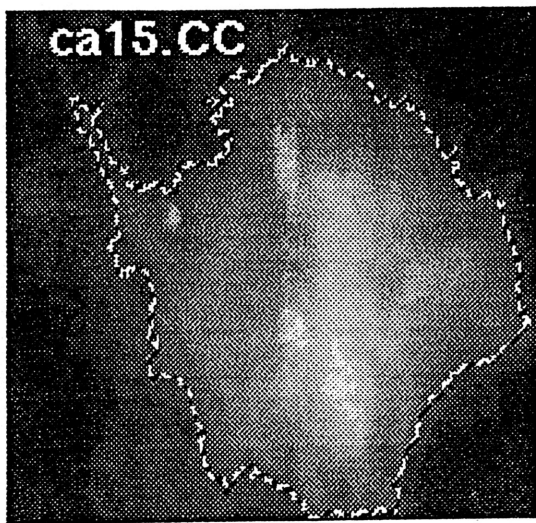
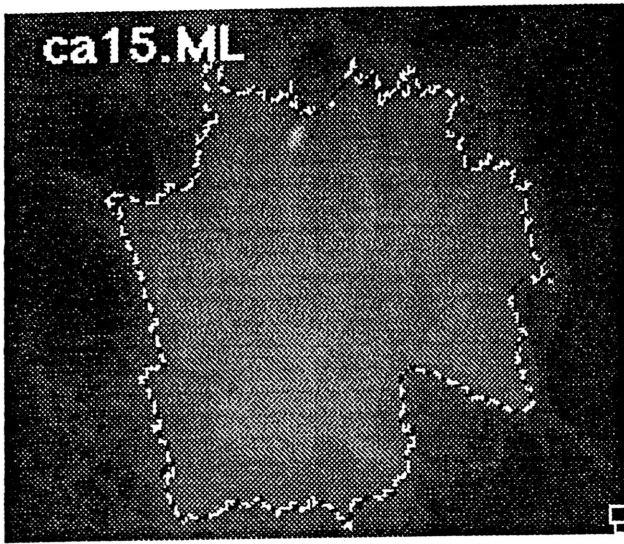


Figure 2. Stellate Carcinoma Segmentation





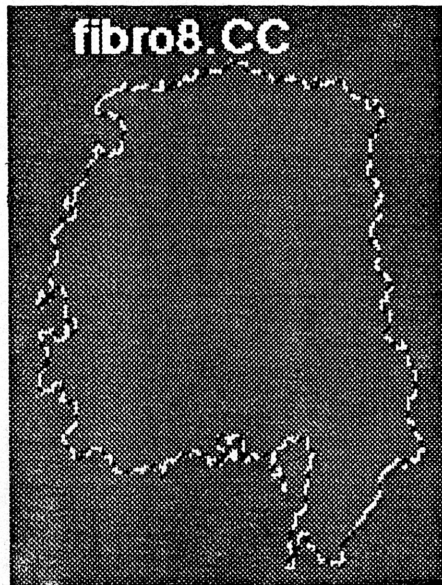
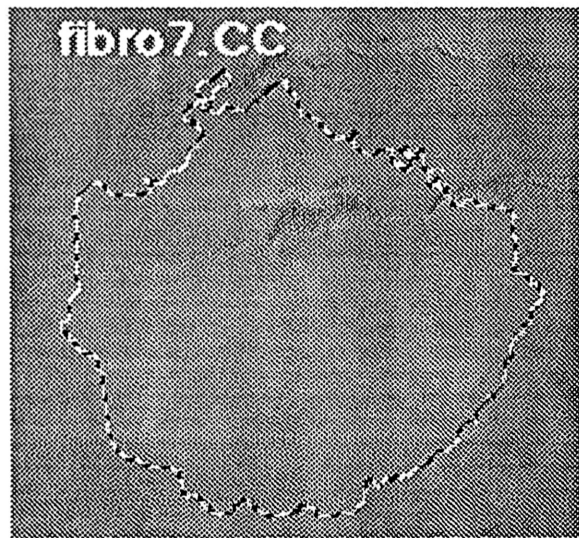
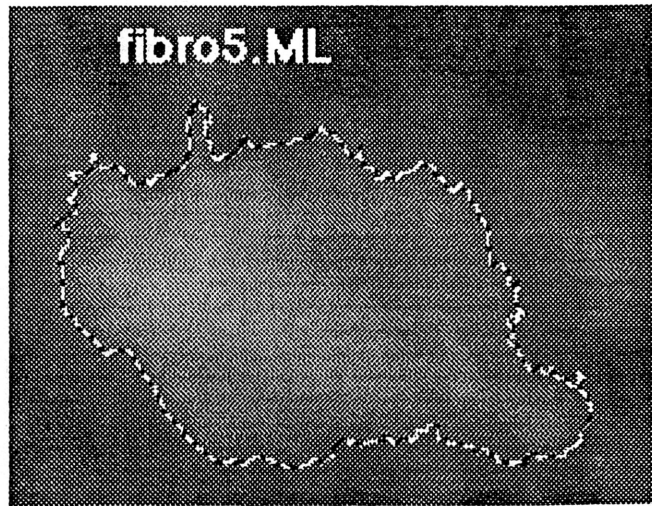
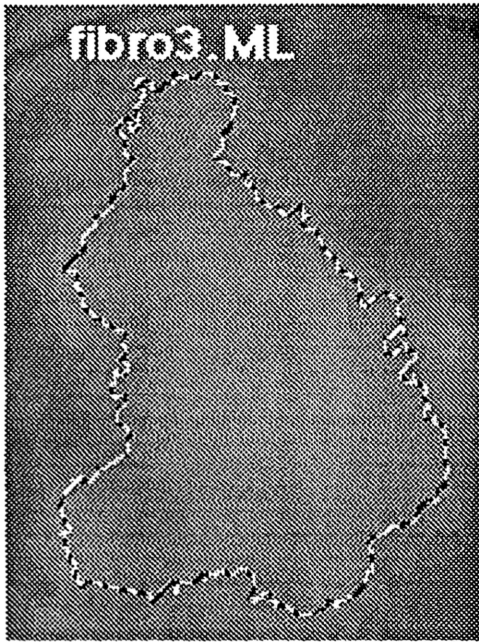
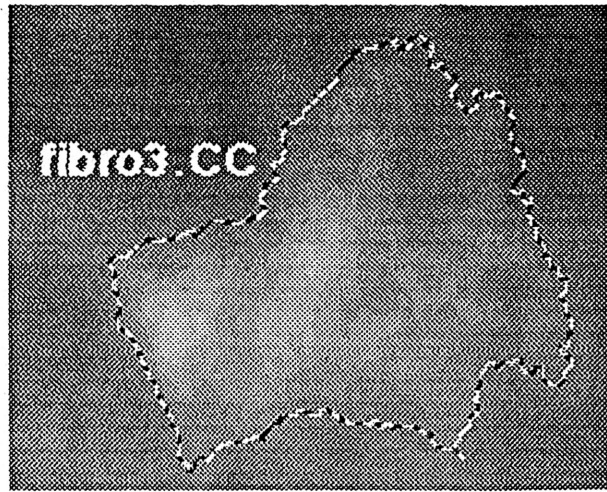
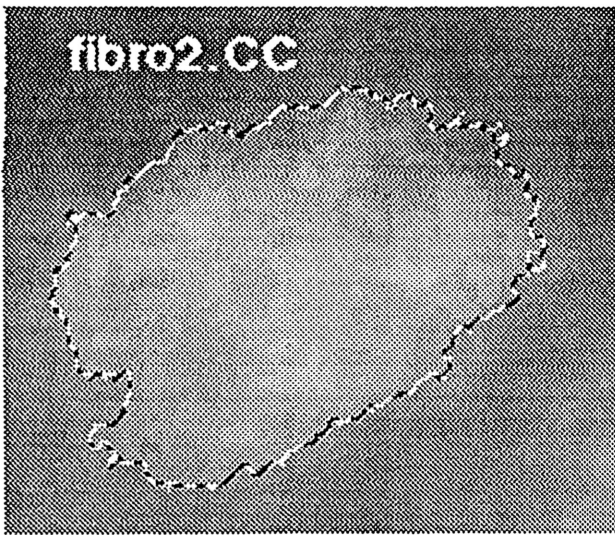
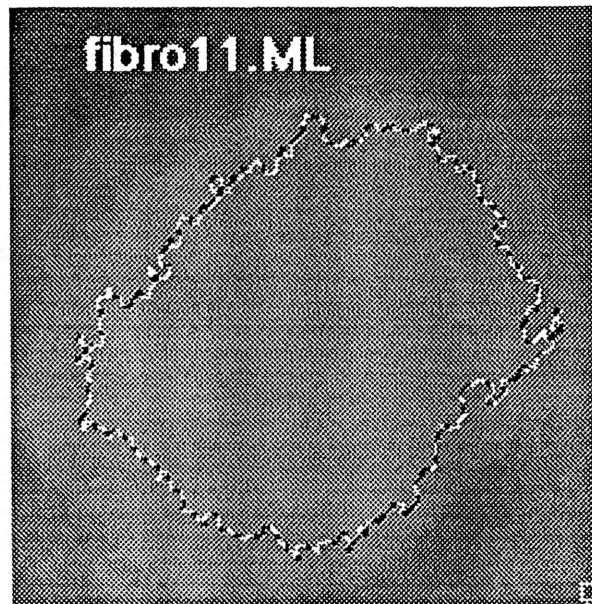
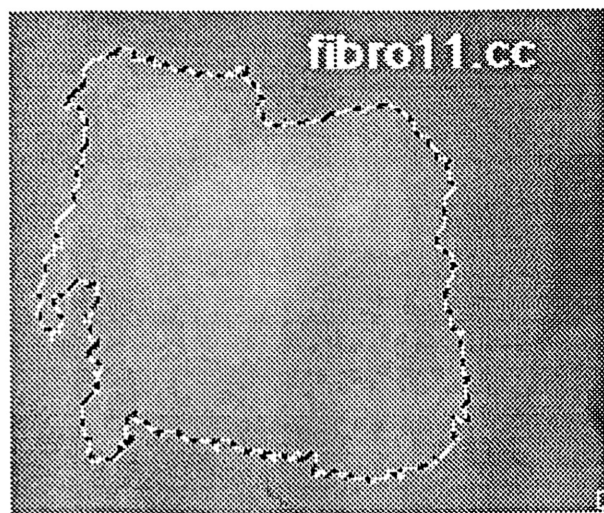
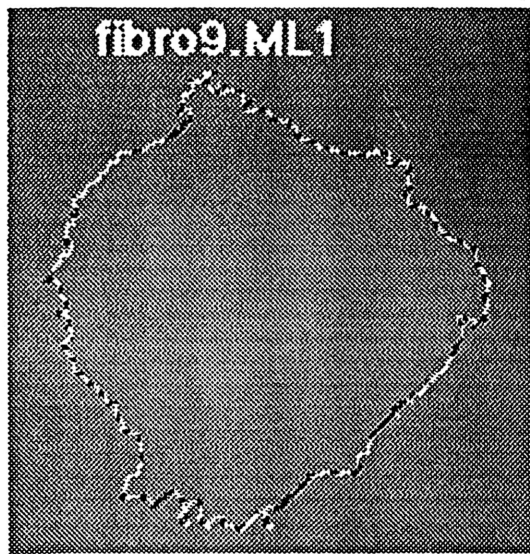
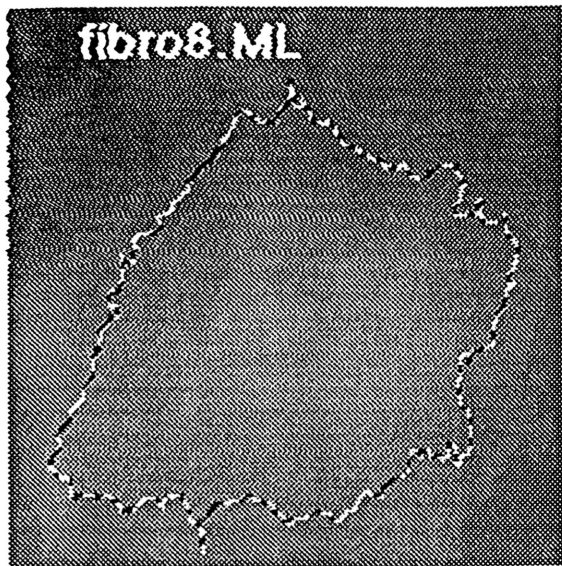
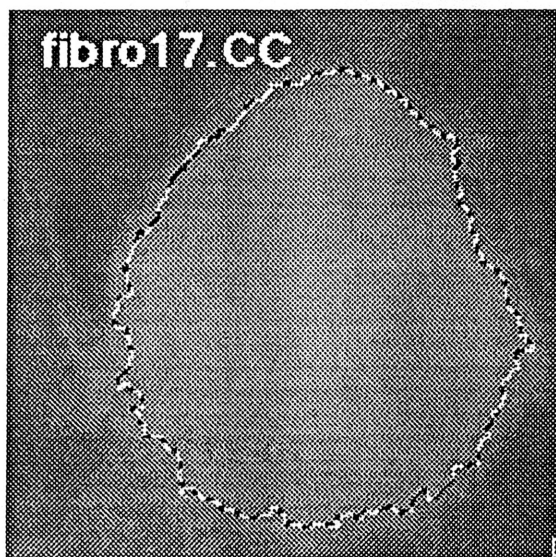
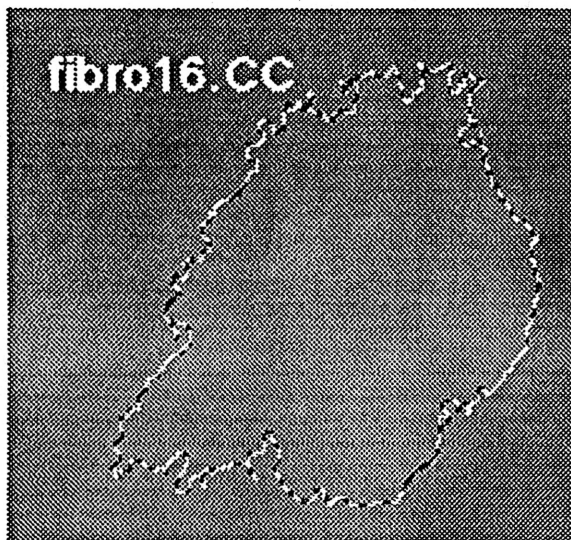
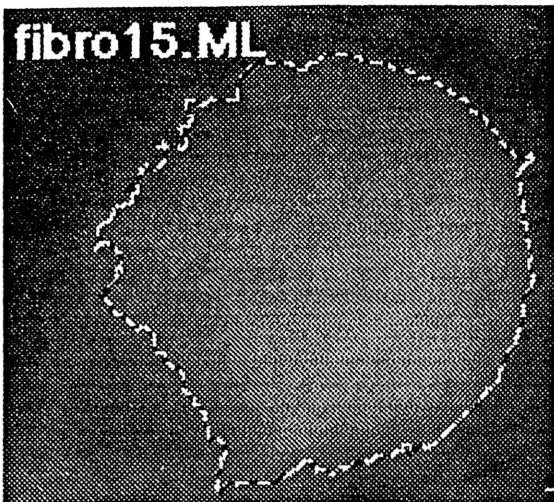
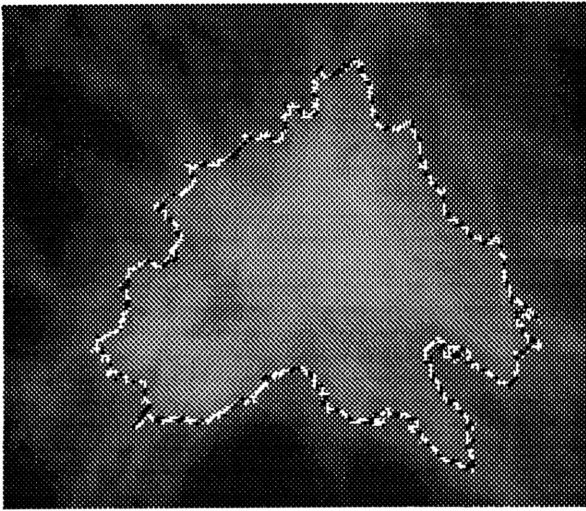


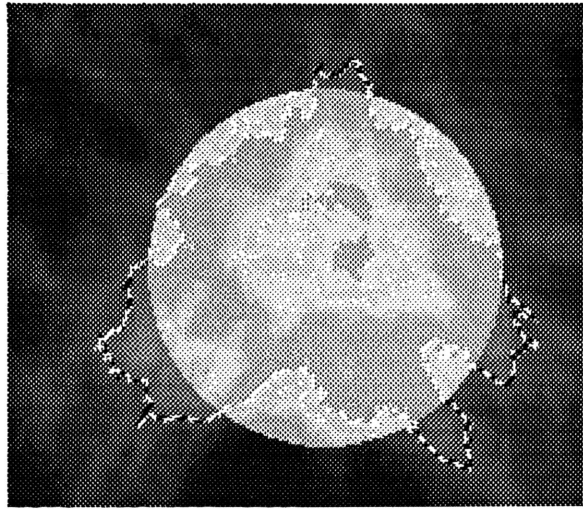
Figure 3. Fibroadenoma Segmentation



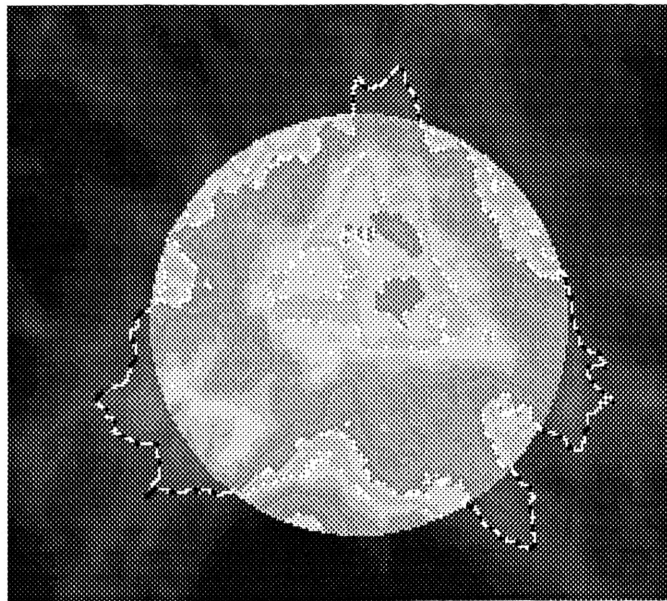




(a)



(b)



(c)

Figure 4

Boundary Plot of Scaled Tumor

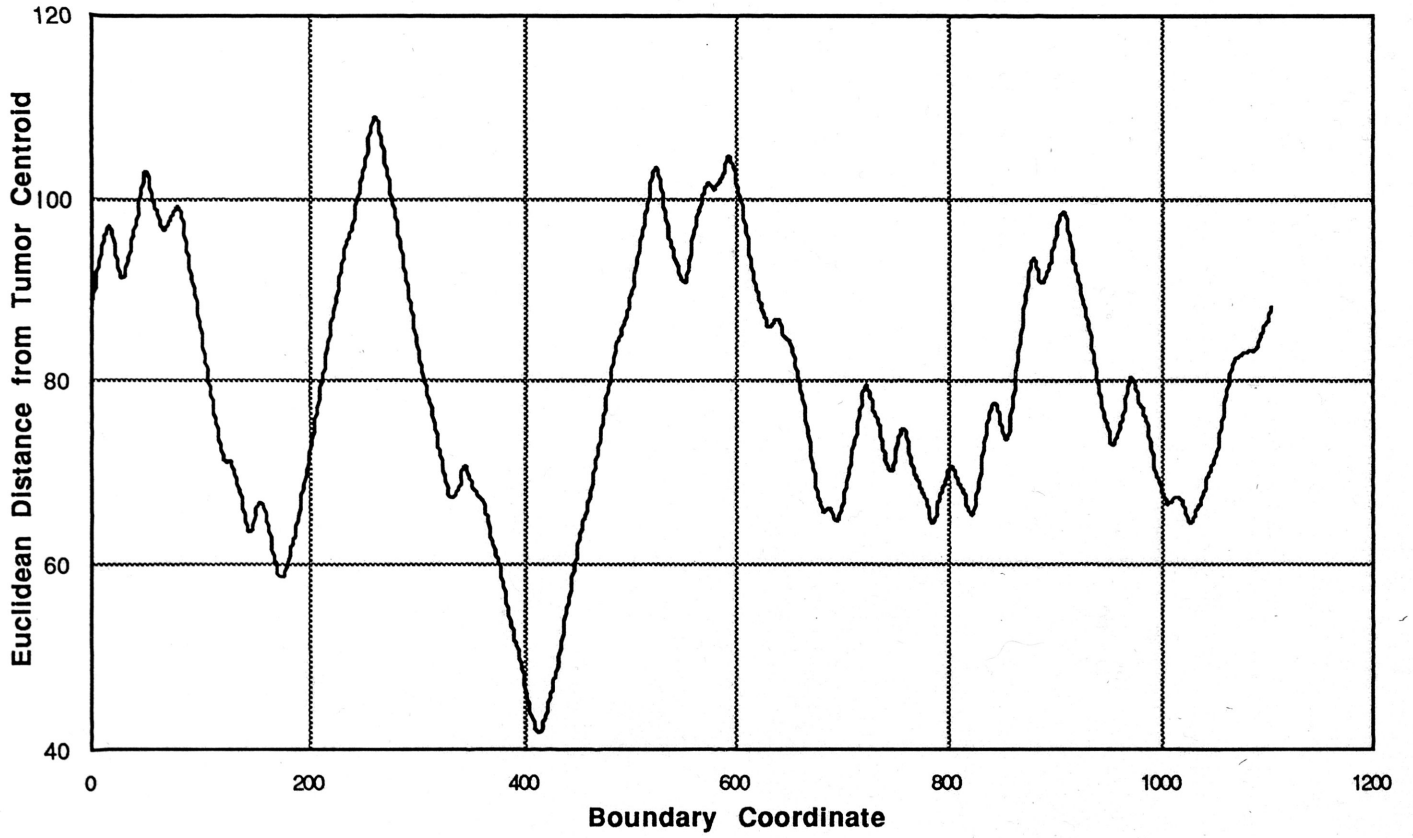


Figure 4. (d)

Sampled Boundary Plot of Scaled Tumor

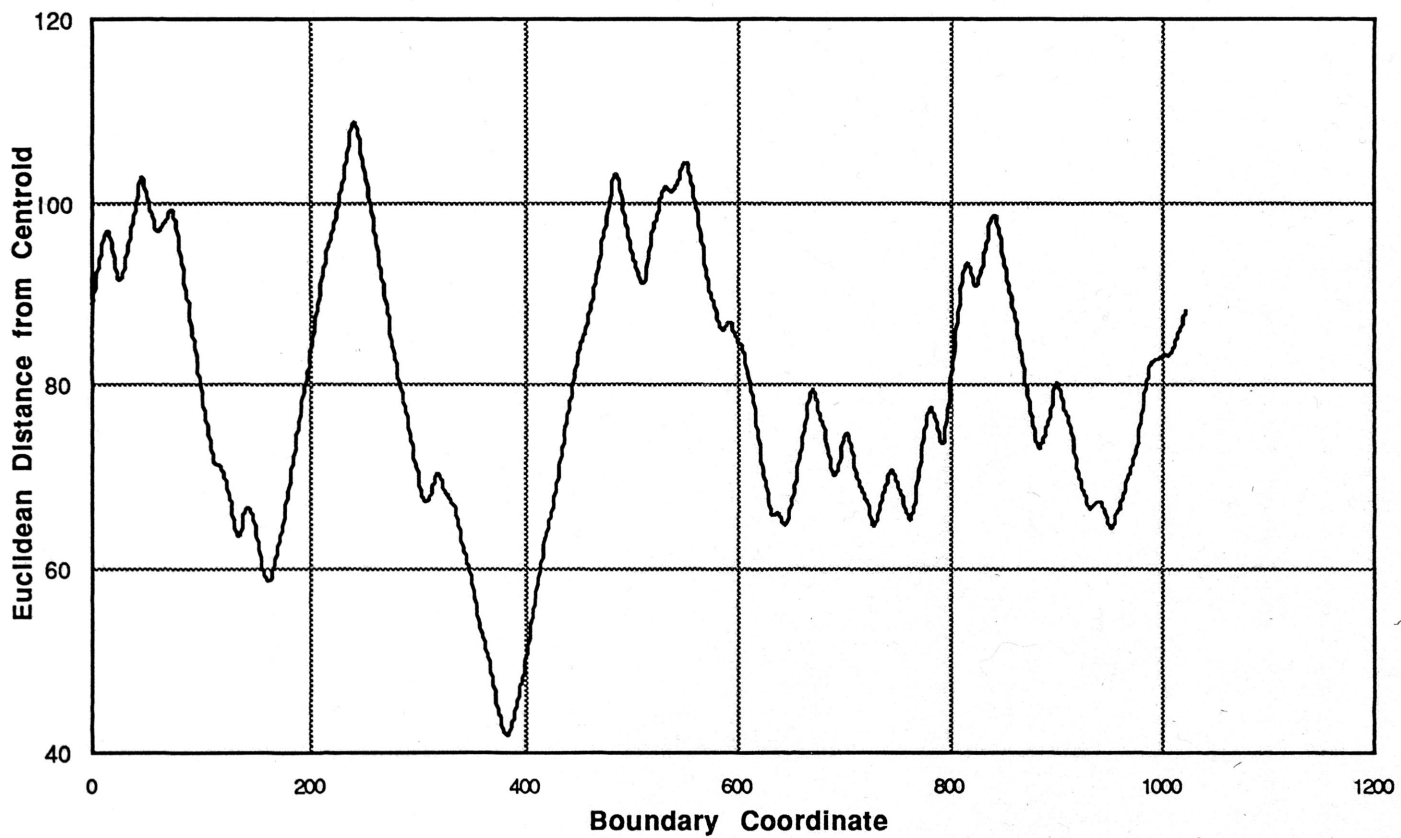


Figure 4. (e)

Fourier Transform of Sampled Boundary Plot

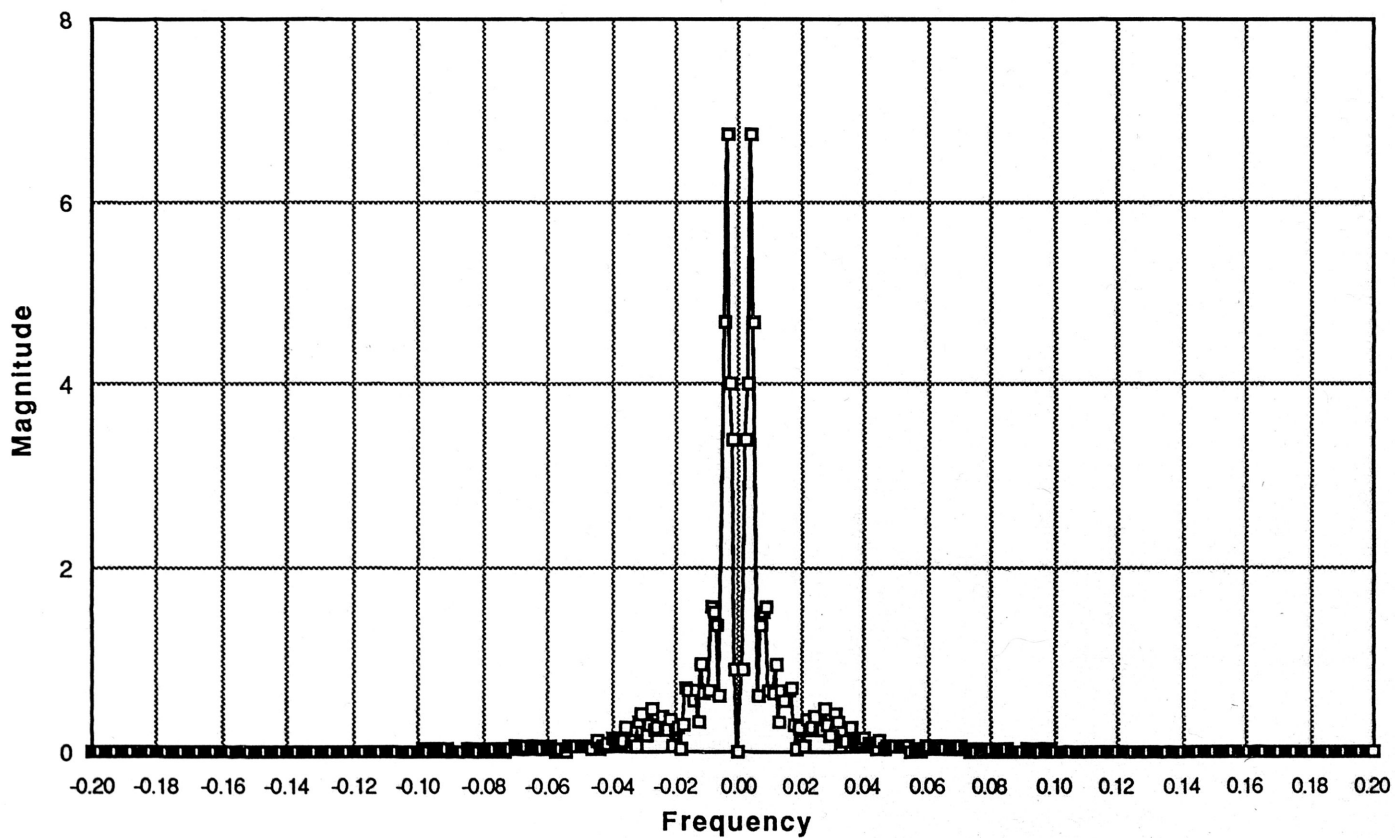


Figure 4. (f)

Tumor Surface Roughness vs. Circularity

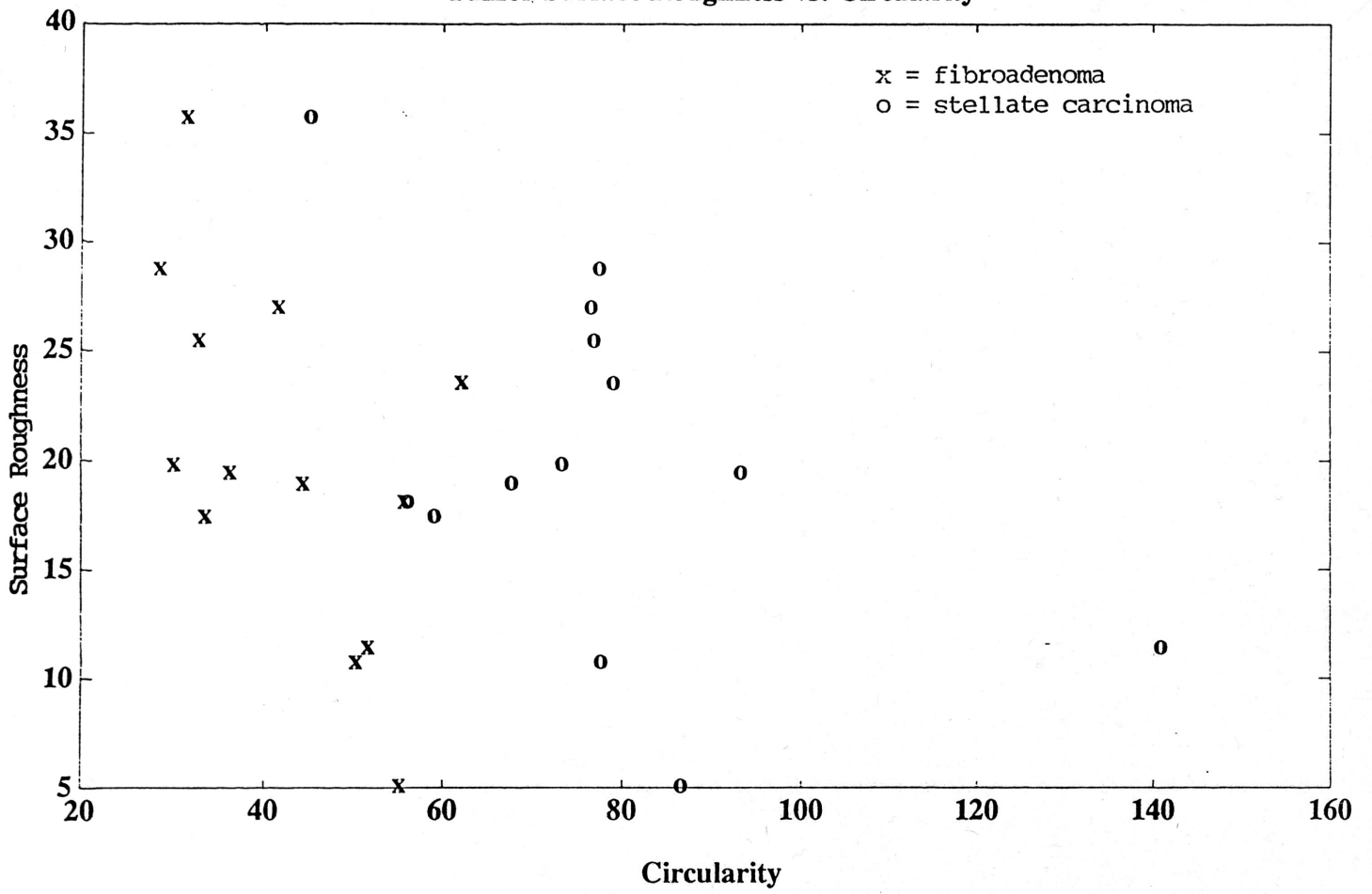


Figure 5.

Tumor Boundary Roughness vs. Circularity

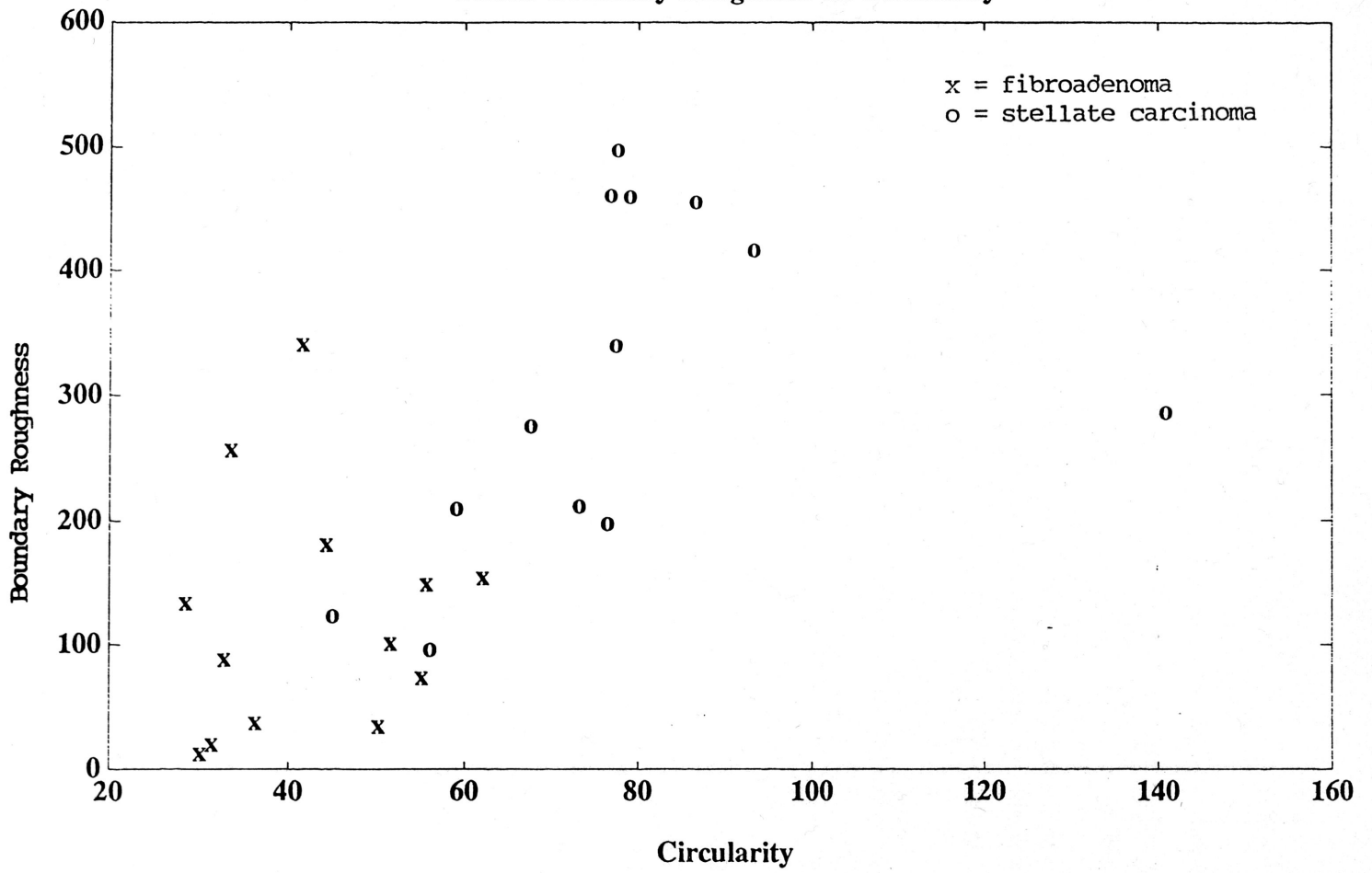


Figure 6.

Tumor Surface Roughness vs. Boundary Roughness

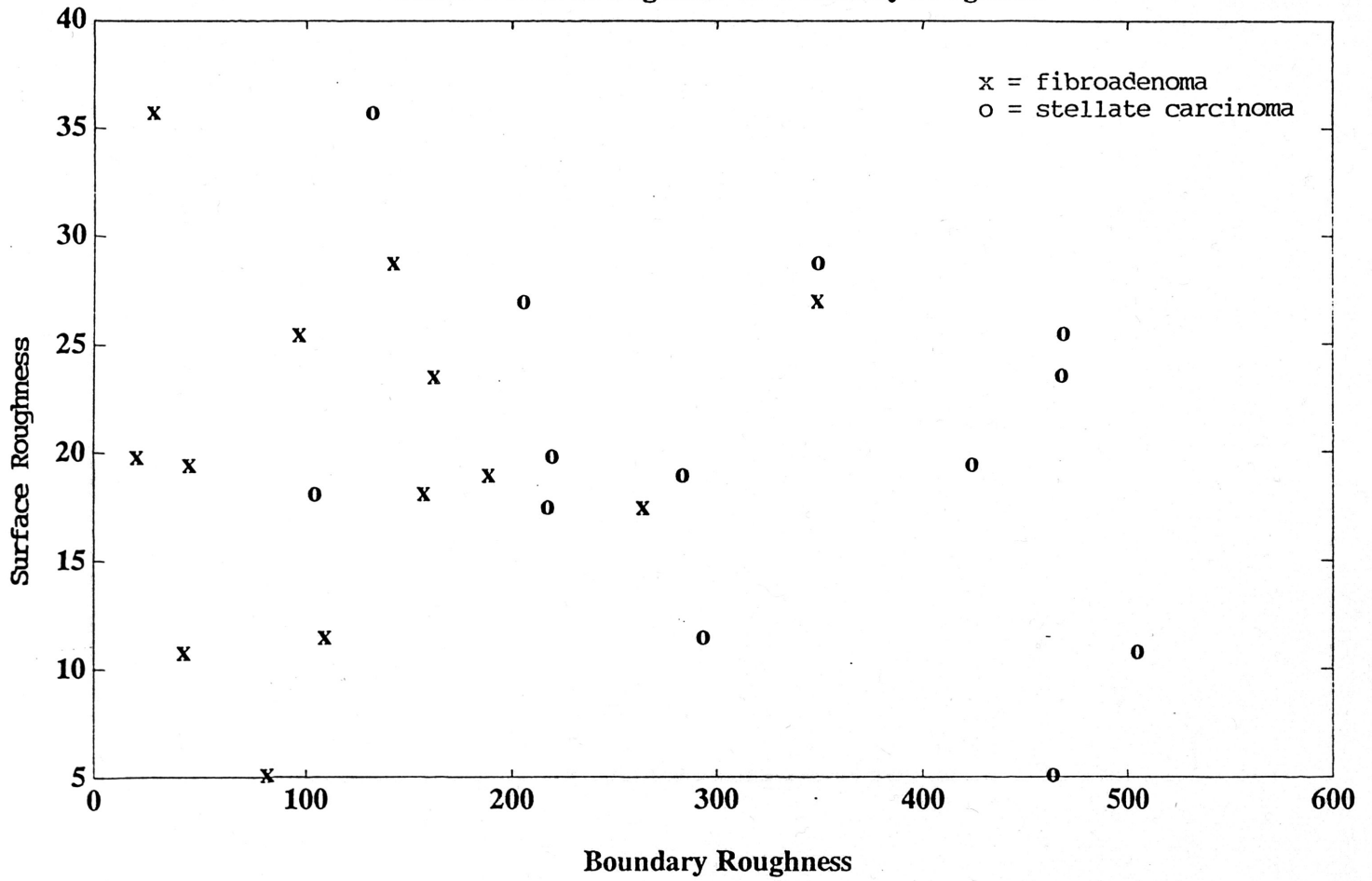
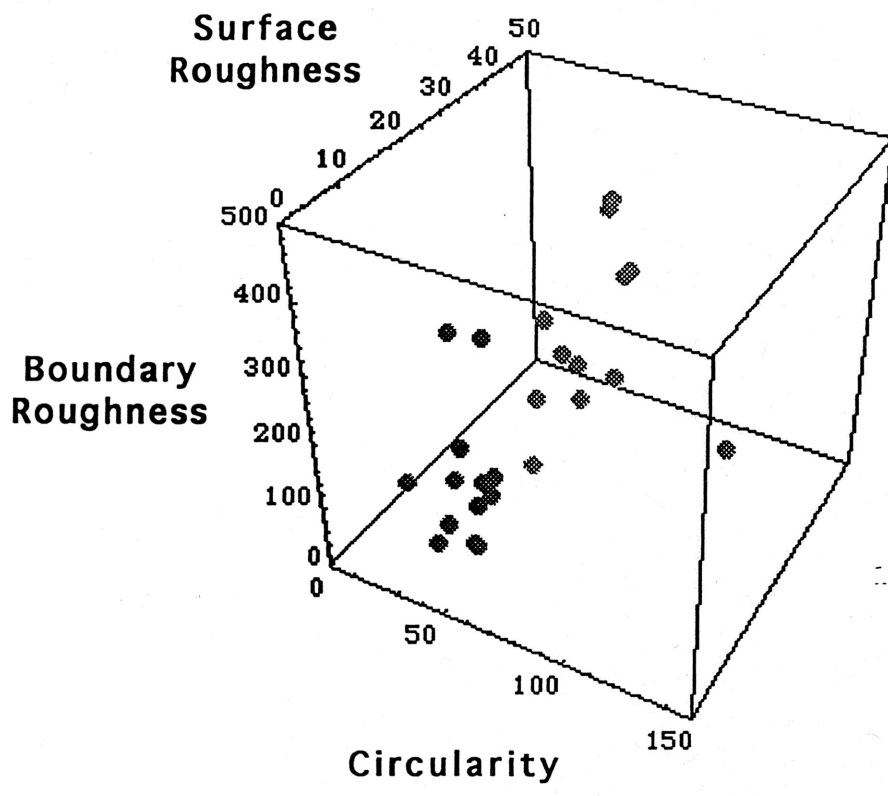


Figure 7.



dark grey = fibroadenoma
 light grey = stellate carcinoma

Figure 8.

STELLATE CARCINOMAS

Image	View	# of Perimeter Points	Area	Parameters of Unscaled Tumor			Scaling Factor	Boundary Roughness
				Average Radius	Circularity	Surface Roughness		
ca1	ML	1635	20953	84.77	77.36	29.23	0.944	348.76
ca1	CC	1495	19906	85.05	67.61	19.45	0.941	283.6
ca3	CC	1579	19222	81.45	76.48	27.47	0.982	205.69
ca3	ML	1181	13865	68.133	59.08	17.94	1.174	217.5
ca10	ML	1789	20187	86.32	93.26	19.94	0.927	424.16
ca12	CC	1881	26882	101.27	78.96	24.01	0.79	467.74
ca12	ML	1767	24244	94.79	76.8	25.95	0.844	468.46
ca13	ML1	1085	9018	58.94	77.62	11.25	1.357	504.86
ca13	CC	1781	13810	69.95	140.94	11.93	1.144	293.68
ca13	ML2	1033	7204	48.41	86.52	5.59	1.653	436.37
ca14	CC	1607	20988	84.65	73.25	20.3	0.945	219.75
ca15	ML	1375	21141	83.21	56.01	18.6	0.961	104.16
ca15	CC	1267	21725	85.75	44.91	36.22	0.933	131.44

X=77.60
SD=22.98

Y=20.61
SD=8.19

Z=315.86
SD=135.65

Table 1.

FIBROADENOMAS

Image	View	# of Perimeter Points	Area	Parameters of Unscaled Tumor			Scaling Factor	Boundary Roughness
				Average Radius	Circularity	Surface Roughness		
fibro2	CC	411	3477	34.16	28.53	4.79	2.342	141.53
fibro3	CC	619	5189	41.81	44.25	8.79	1.913	188.87
fibro3	ML	623	5480	43.41	41.54	9.34	1.843	348.52
fibro5	ML	481	3999	37.15	33.56	19.83	2.153	264.28
fibro7	CC	707	8478	51.98	36.31	6.20	1.539	44.99
fibro8	CC	689	4656	39.15	62.14	5.95	2.043	161.64
fibro8	ML	475	4399	38.09	32.87	12.09	2.100	96.43
fibro9	ML1	947	10937	60.48	50.12	8.51	1.323	42.23
fibro11	CC	943	10158	57.1	51.53	8.29	1.401	109.14
fibro11	ML	779	6668	46.67	55.11	5.38	1.714	81.73
fibro15	ML	865	14728	68.67	30.15	22.19	1.165	20.25
fibro16	CC	639	4321	38.81	55.65	7.86	2.061	156.58
fibro17	CC	947	17118	73.82	31.45	11.02	1.084	27.80

X=52.07
SD=11.35

Y=10.02
SD=5.34

Z=129.54
SD=96.78

Table 2.